Petroleum Science 23 (2026) 7266–7281

Contents lists available at ScienceDirect

Petroleum Science

journal homepage: www.keaipublishing.com/en/journals/petroleum-science

Original Paper

Study on flow regimes of blocky proppant dunes in rough fractures based on CFD-DEM method

Zhi-Chao Yang [a], Meng-Meng Zhou [a,*], Wen-Zhao-Yang Xie [a], Xian-Zhi Song [a], Zheng-Ming Xu [b]

[a] National Key Laboratory of Petroleum Resources and Engineering, China University of Petroleum (Beijing), Beijing, 102249, China
[b] School of Energy Resources, China University of Geosciences, Beijing, 100083, China

ARTICLE INFO

Article history:
Received 19 May 2025
Received in revised form
12 February 2026
Accepted 6 July 2026
Available online 21 July 2026

Edited by Jia-Jia Fei

Keywords:
Hydraulic fracturing
Proppant transport
CFD-DEM
Rough fracture
Flow regimes

ABSTRACT

Enhancing the efficiency of hydraulic fracturing is crucial in developing unconventional reservoirs, where fracture roughness commonly arises and strongly affects proppant transport behavior. However, it often results in rough fractures that accompany various problems. Addressing these issues, a validated computational fluid dynamics-discrete element method (CFD-DEM) approach was employed, and a narrow rough fracture model was developed using the spectral synthesis method to investigate proppant transport during hydraulic fracturing. Initially, the model was validated against previous research, followed by examining the relationship between changing flow regimes and force characteristics compared to continuous fractures. The impact of injection velocity, fracture inclination angle, and fluid viscosity on flow regimes and micro-internal mechanisms was also analyzed. The findings reveal distinct flow regimes and force characteristics of blocky dunes compared to continuous dunes. Notably, the drag force curve exhibits two stages in the proppant transport process: the settlement-dominant and scour-dominant stages. Furthermore, the results indicate two micro-mechanisms for improving proppant transport efficiency: reducing particle–particle interaction forces and prolonging particle settling time, the latter of which can be effectively achieved by increasing fluid viscosity. Finally, a multi-factor analysis based on an orthogonal test method is conducted to evaluate the combined influence of key parameters. This study significantly advances our understanding of proppant transport in rough fractures and offers valuable insights for optimizing injection parameters.

© 2026 The Authors. Publishing services by Elsevier B.V. on behalf of KeAi Communications Co. Ltd. This is an open access article under the CC BY license (http://creativecommons.org/licenses/by/4.0/).

1. Introduction

With conventional oil and gas reserves being depleted and increasingly challenging to exploit, unconventional reservoirs, whose reserves are large and widely distributed, need to be developed (Bai et al., 2021; Budiman et al., 2025). Since oil and gas are usually stored in reservoir pores, developing them is challenging (Detournay, 2016; Wen et al., 2024).

Hydraulic fracturing is a universal technology that generates complex fractures to improve reservoir conductivity (Barboza et al., 2021; Chen et al., 2022; Li et al., 2023). To maintain the fractures' conduct effect, injection proppant is crucial to support the fractures so they cannot be closed (Song et al., 2024). Due to the project's complexity and invisibility, the proppant transport behavior and changes within the fractures are still unclear (Li et al., 2023). At the same time, its multi-factor influencing characteristics and inherent transport mechanism need to be explored.

Currently, there are two main methods to study proppant transport: experimentation and simulation (Kuang et al., 2020). Experimentation is the more direct method observing proppant transport in the fractures (Huang et al., 2024). Kern et al. (1959) constructed a fracture using two parallel plates for the first time. However, the simplified fracture model may not restore the fracture characteristics of the underground very well. Subsequent scholars made improvements and performed experimental optimizations on this basis. Li et al. (2017) and Wen et al. (2016) investigated different variables' impact on balance proppant placement in the complex-fracture networks. Basiuk et al. (2022) designed different outlets and focused on the characteristics of

* Corresponding author.
E-mail address: zhoumm@cup.edu.cn (M.-M. Zhou).
Peer review under the responsibility of China University of Petroleum (Beijing).

https://doi.org/10.1016/j.petsci.2026.07.012
1995-8226/© 2026 The Authors. Publishing services by Elsevier B.V. on behalf of KeAi Communications Co. Ltd. This is an open access article under the CC BY license (http://creativecommons.org/licenses/by/4.0/).

placement dunes. Qu et al. (2021) designed a tortuous fracture to investigate the proppant transport and found the transport behavior is more complex than the straight fractures. Rough fractures, closer to real fractures, have become a current research focus (Gong et al., 2023). Huang et al. (2018) captured the rock surface characteristic as a rough fracture surface and observed the proppant transport with different initial conditions. Li et al. (2021) used 3D printing technology to construct rough fractures, where many special patterns merge and differ from smooth fractures. The proppant placement in rough fractures greatly differs from the smooth fractures. However, the comprehensive flow regime changes and its mechanism needs simulation to be illustrated.

Simulation is another important method that can overcome the experiment's disadvantages (Zheng et al., 2020), data acquisition difficulties, and microanalysis limitations (Lv et al., 2024). Proppant transport is a typical liquid–particle two-phase flow problem. Two common methods are used for proppant transport in rough fractures: the Eulerian-Eulerian and Eulerian-Lagrangian methods, which are based on the computational fluid dynamics (CFD) method (Li et al., 2024a; Qu et al., 2022). In the Eulerian-Eulerian method, both liquid and solid phases are treated as continuum media and solved by Navier-Stokes equations (Liu et al., 2025; Zhang et al., 2023). It has a relatively simplified calculation and requires fewer computing resources (Zhou et al., 2020, 2021). Therefore, it is widely applied. Some scholars have used this method to understand proppant transport (Suri et al., 2019). In the Euler-Lagrange method, the liquid phase is modeled as continuous, and the solid phase is simulated as discrete (Tang et al., 2022). Through this method, the particle–particle and particle–wall collisions, which are real, exists, and has a great effect on the energy transferred, can be modeled (Kuang et al., 2020). The latter can compute more accurately than the former (Zhang et al., 2022). The computational fluid dynamics-discrete element method (CFD-DEM) is based on the Eulerian-Lagrangian method (Akhshik et al., 2016). It directly tracks the trajectories and forces acting on each particle with greater proven accuracy (Kuang et al., 2020). There are many works in rough fractures based on the CFD-DEM method (Gong et al., 2023; Li et al., 2024b; Zheng et al., 2025a, 2025b). Feng et al. (2018) used the CFD-DEM method to investigate the proppant transport and plugging process in rough fractures. Zheng et al. (2023) applied the CFD-DEM method and considered the impact of proppant size and wall roughness (fractal dimension and RMS (root mean square) value) on the proppant placement in rough fracture with fracturing fluid of supercritical CO_2. Guo et al. (2022) analyzed the rough branch fractures and adjusted the inclination angle of the secondary branched fracture to evaluate the transport capacity by the CFD-DEM method.

Many scholars focus on dune development. Tong and Mohanty (2016) used a single branch fracture to examine the proppant placement. They found three regions during the injection process: the bottom immobile sand bed zone, the middle flowing slurry zone, and the top clear fluid zone. Zheng et al. (2020) and Zhou et al. (2024) found that dune development has three stages: flat laying, proppant dune, and proppant bank development. Huang et al. (2020) found two types of patterns in rough fractures: sand-dune settling patterns and tree-like settling patterns. Xiao et al. (2025) demonstrated that fracture surface roughness and micro-protrusion geometry impact the maximum proppant placement distance and dune morphology, providing further insight into the interaction between roughness and sedimentation patterns. However, they have not thoroughly studied the causes of its formation at the micro level or in mechanics.

The fracture inclination angle is an important factor that should be considered in real hydraulic fracturing angle (Sahai and Moghanloo, 2019). Broadly, the fracture inclination is a branch fracture variable used in interaction between the main fracture and secondary fracture (Guo et al., 2022; Li et al., 2018) or an incline angle in tortuous fractures (Li et al., 2023, 2024b; Li et al., 2023; Qu et al., 2021). At the same time, many scholars analyzed the inclined fracture direction with gravity direction. Ba Geri et al. (2018) designed an inclined fracture for the experiment and compared the proppant transport behavior with vertical hydraulic fracturing. Kou et al. (2018) used the CFD-DEM method to simulate the different inclining angle fractures and found the two processes, the suspension stage, and settling stage, in inclined fractures, and the placement efficiency is better than in vertical fractures. Zhang et al. (2022) simulated the flat rough fractures with different incline angles and evaluated the placement shape. But they limited in the initial time. Chun et al. (2020) analyzed the inclined fracture experiment with three injection inlets. The results indicate less proppant in the inclined fracture can quickly occupy a more efficient area. However, they do not consider the micro mechanism and roughness effect.

Blocky proppant dunes, which typically form in rough fractures, refer to discontinuous and segmented proppant accumulations characterized by irregular geometry and distinct gaps between adjacent dune bodies. These blocky dunes represent an important morphological feature for evaluating proppant placement and dune shape in rough fracture conditions. Li et al. (2021) found blocky dunes in rough fractures through their experiment, and they described the dunes as finger-like piling. The dunes have traits such as particle wormholes, cavities, and isolated pillars in their description. Huang et al. (2017, 2018, 2020) investigated the proppant transport in rough fractures and found blocky dunes in their experiment. Zheng et al. (2023), Zhou et al. (2024) and Yin et al., (2023) also found this special phenomenon in their simulation based on the CFD-DEM method, but they didn't analyze the flow regimes and their internal force structure mechanism. Song et al. (2024) used CFD-DEM analyzed the blocky dunes' generation condition and found the ratio of proppant size to fracture width is the key factor. Yang et al. (2024) used CFD-DEM method examined the blocky dunes' generation and collapse of local sand plugs, which phenomenon is also observed in Huang et al.'s work (Huang et al., 2024). Therefore, as an important and common type of dune, it is necessary to study the blocky dunes' flow regimes.

This paper uses a validated CFD-DEM model to study the flow regimes of blocky proppant dunes in rough narrow fractures, with particular emphasis on their unique placement behavior and pressure drop characteristics. To gain insight into the distinct micro-scale force mechanisms governing blocky dune formation and transport, a detailed force analysis is conducted. Firstly, a systematic comparison is performed between smooth fractures with continuous dunes and rough fractures with blocky dunes, highlighting the differences in flow regimes and force characteristics. Then, the effects of injection velocity, fracture inclination angle, and fluid viscosity on blocky proppant dune placement and force evolution are investigated to clarify their influence on proppant transport efficiency. Finally, a multi-factor analysis based on an orthogonal test method is conducted to identify the dominant factors controlling proppant transport behavior.

2. Methodology and computational details

2.1. Particle phase

In the DEM method, for particles, their trajectories are explicitly solved by Lagrangian tracking in the computational domain. The

translation and rotation of particle i are governed by Newton's second law, as expressed in the following equation:

$$m_i\frac{\mathrm{d}\boldsymbol{v}_i}{\mathrm{d}t}=m_i\boldsymbol{g}+\boldsymbol{f}_{\mathrm{fp},i}+\sum_{j=1,j\neq i}^{k}\boldsymbol{f}_{\mathrm{c},ij} \tag{1}$$

$$I_i\frac{\mathrm{d}\boldsymbol{\omega}_i}{\mathrm{d}t}=\sum_{j=1}^{k}\boldsymbol{T}_{ij} \tag{2}$$

where $\boldsymbol{v}_i$ is the velocity of particle i, g is the gravitational acceleration, $\boldsymbol{f}_{\mathrm{fp},i}$ is the fluid–particle interaction force acting on particle i, and $\boldsymbol{f}_{\mathrm{c},ij}$ is the contact force exerted by particle or wall j on particle i. I_i is the moment of inertia of the particle, $\boldsymbol{\omega}_i$ is the rotational velocity of particle i, $\boldsymbol{T}_{ij}$ is the total torque between particle i and particle/wall j, respectively. The total external force acting on the particle $\boldsymbol{F}_i$ is given by

$$\boldsymbol{F}_i=\boldsymbol{F}_{\mathrm{C},i}+\boldsymbol{F}_{\mathrm{D},i}+\boldsymbol{F}_{\mathrm{LS},i}+\boldsymbol{F}_{\mathrm{LM},i}+\boldsymbol{F}_{\mathrm{CO},i} \tag{3}$$

where $\boldsymbol{F}_{\mathrm{C},i}$ is the contact force, $\boldsymbol{F}_{\mathrm{D},i}$ is the drag force, $\boldsymbol{F}_{\mathrm{LS},i}$ is the Saffman lift force, $\boldsymbol{F}_{\mathrm{LM},i}$ is the Magnus lift force, and $\boldsymbol{F}_{\mathrm{CO},i}$ is the cohesive force. Previous research has sufficiently analyzed various forces, so we skip detailed explanations here. The proppants are assumed to be spherical particles with a diameter of 0.6 mm and a density of 2650 kg/m^3, which are kept constant throughout the simulations.

2.2. Fluid phase

For an incompressible fluid phase with a secondary particulate phase, the governing equations of mass and momentum conservation for the liquid flow introduced by the flow characteristics are expressed as (Gidaspow, 1994; Zhou et al., 2020, 2022):

$$\frac{\partial}{\partial t}\left(\varepsilon_{\mathrm{f}}\rho_{\mathrm{f}}\right)+\nabla\cdot\left(\varepsilon_{\mathrm{f}}\rho_{\mathrm{f}}\boldsymbol{u}_{\mathrm{f}}\right)=0 \tag{4}$$

$$\frac{\partial}{\partial t}\left(\varepsilon_{\mathrm{f}}\rho_{\mathrm{f}}\boldsymbol{u}_{\mathrm{f}}\right)+\nabla\cdot\left(\varepsilon_{\mathrm{f}}\rho_{\mathrm{f}}\boldsymbol{u}_{\mathrm{f}}\boldsymbol{u}_{\mathrm{f}}\right)=-\varepsilon_{\mathrm{f}}\nabla p+\nabla\left(\varepsilon_{\mathrm{f}}\rho_{\mathrm{f}}\boldsymbol{\tau}\right)+\varepsilon_{\mathrm{f}}\rho_{\mathrm{f}}\boldsymbol{g}+\boldsymbol{F}_{\mathrm{pf}} \tag{5}$$

where, $\boldsymbol{u}_{\mathrm{f}}$ denotes the fluid velocity; ρ_{f} represents the fluid density, and ε_{f} corresponds to the volume fraction of the pure fluid within the computational cell, ∇p is the pressure gradient of the fluid; $\boldsymbol{\tau}=\mu\nabla\boldsymbol{u}_{\mathrm{f}}$ is the fluid stress tensor; μ is the viscosity of the fluid; $\boldsymbol{F}_{\mathrm{pf}}$ is the volumetric fluid–solid interaction force and calculated by (Zhou et al., 2010):

$$\boldsymbol{F}_{\mathrm{pf}}=-\frac{1}{V_{\mathrm{cell}}}\sum_{i=1}^{k_{\mathrm{c}}}\left(\boldsymbol{f}_{\mathrm{drag},i}+\boldsymbol{f}_{\mathrm{lift},i}+\boldsymbol{f}_{\mathrm{add},i}\right) \tag{6}$$

where k_{c} is the number of particles in a computational cell; $\boldsymbol{f}_{\mathrm{drag},i}$ is the fluid drag force; $\boldsymbol{f}_{\mathrm{lift},i}$ is the lift force and $\boldsymbol{f}_{\mathrm{add},i}$ is the added mass force.

2.3. Phase coupling

For small particles, fluid–particle interactions are analyzed at the fluid-element level. The fluid velocity field should be transmitted from the CFD side to the DEM side. In DEM, each particle's drag needs updating as it relates to local fluid velocity. Conversely, particle velocities and positions should be transmitted from the DEM side to the CFD side. In CFD, the drag term from particles and fluid volume fraction need updating. The coupling of the two is achieved by integrating the void fraction term and the fluid–particle interaction force, which are spatially correlated based on their positions (Zhou et al., 2020). The void fraction ε_{f} is expressed as (Gui et al., 2008):

$$\varepsilon_{\mathrm{f}}=1-\sum_{i}^{N}V_{\mathrm{p},i}\Big/V_{\mathrm{cell}} \tag{7}$$

where, V_{cell} is the volume of the computational cell; N is the number of particles in the cell; $V_{\mathrm{p},i}$ is the volume of the particle.

2.4. Computational details

2.4.1. Numerical model verification

The model has been verified for simulating proppant transport within fractures, with detailed discussions provided in previous papers (Song et al., 2024; Yang et al., 2024; Zhou et al., 2024). The following is a concise summary. To validate the model, key parameters of dunes from existing experiments were compared with those of this model, using the proppant placement experiment described in Tong and Mohanty (2016) as a reference. In this experiment, slurry entered through an inlet on the right side, and proppant placement was observed at 20, 40, and 60 s, as shown in Fig. 1(a). The simulation was conducted under the same boundary conditions as the experiment, and the corresponding placement results at each time point are shown in Fig. 1(b). It can be observed that the morphologies are largely similar. Additionally, the errors in specific characteristic parameters of the dunes, such as DPBH (dimensionless proppant bank height) and DPBL (dimensionless proppant bank length), are less than 2%, which are signed on the figure. This demonstrates the effectiveness of this model in simulating proppant transport.

2.4.2. Rough fracture models generation and boundary condition

The generation process of rough fractures is consistent with that reported in previous studies (Song et al., 2024; Yang et al., 2024; Zhou et al., 2024). The fracture model is the same as the model in Yang et al. (2024), including the size and key roughness parameters, fractal dimension and standard deviation. The model was generated by a method of synthesizing fractures proposed by Ogilvie et al. (2006). This method is based on spectral synthesis method (Ogilvie et al., 2006). Many scholars have used it for the study of numerical simulation fracture models (Gong et al., 2023; Guo et al., 2022; Suri et al., 2019; Yamashiro and Tomac, 2022; Zheng et al., 2023).

To obtain better calculation efficiency and accuracy, structured grid division is adopted. The final generated rough fracture model and grid division front view are revealed in Fig. 2(a). The slurry enters from the left side of the fracture and transports along the y-direction toward the depth of the fracture.

Fig. 2(a) also depicts the arrangement of boundary conditions. In the CFD model, a constant velocity inlet is defined, paired with a zero-pressure outlet and no-slip walls. For the DEM model, particles enter the fracture at a uniform velocity, with fixed boundaries ensuring that particles are confined within the specified domain. Particles that reach the boundary undergo a rebound effect. This configuration of boundary conditions provides a more accurate representation of the transport behavior of proppants within the fracture. Based on the above micro-scale force analysis and flow regime classification, the applicability of the present numerical results to field-scale hydraulic fracturing operations is discussed. Although the simulations are conducted at a laboratory scale, the essential physical mechanisms governing proppant transport in rough fractures are preserved through geometric similarity and force balance considerations. In particular, the relative contributions

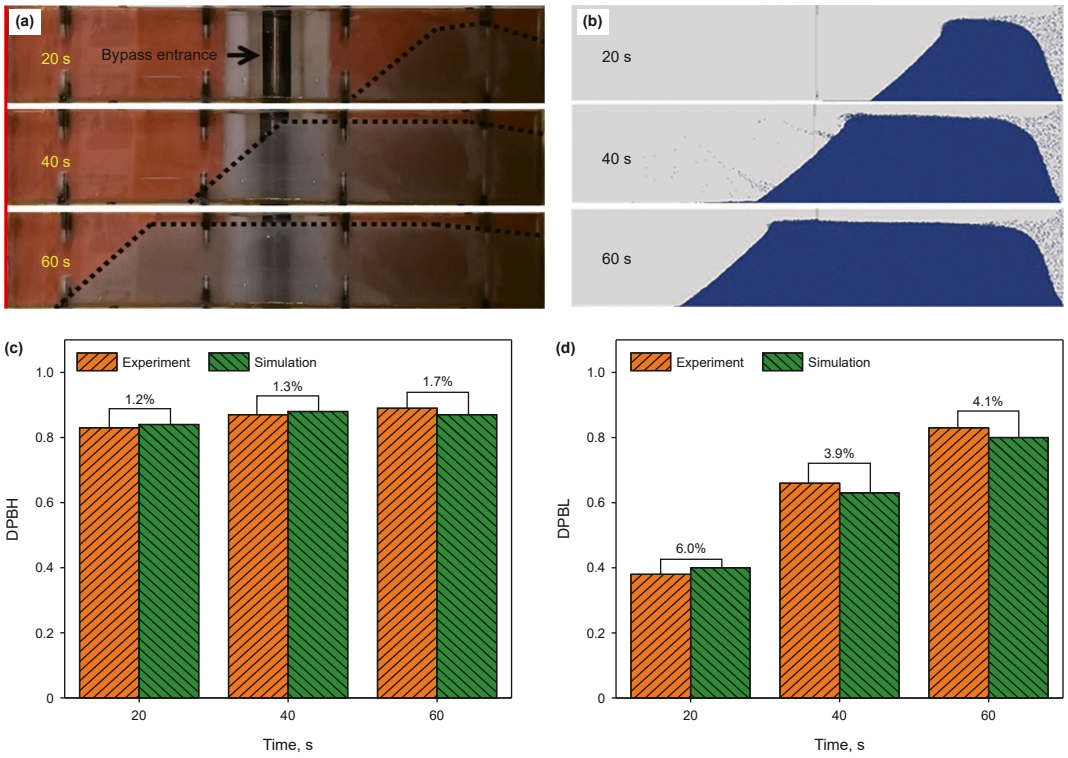


Fig. 1. Comparison of proppant placement between simulation and experiment at different times and validation of key influencing factors: (**a**) Tong and Mohanty's experiment (Tong and Mohanty, 2016); (**b**) simulation; (**c**) DPBH; (**d**) DPBL.

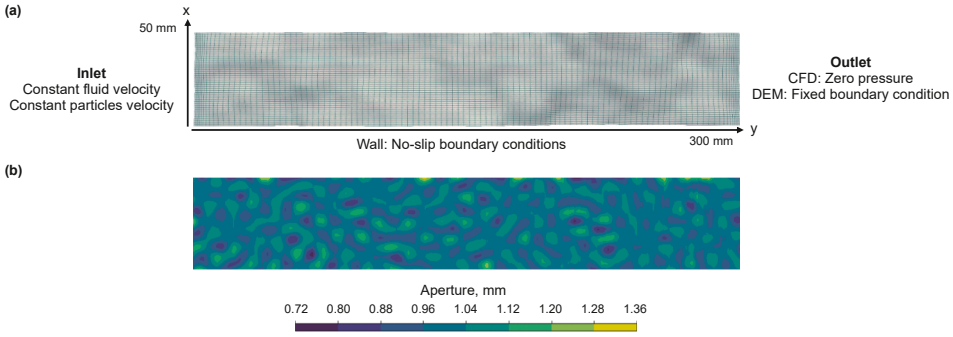


Fig. 2. (**a**) Grid division of narrow rough fracture model and boundary conditions. (**b**) Description of the fracture aperture.

of gravity, fluid drag, and particle–particle interactions control the formation and evolution of blocky proppant dunes, and these mechanisms are not inherently dependent on the absolute fracture size. Fig. 2(b) illustrates the description of the fracture aperture with an average aperture value set to 1 mm.

In addition to the above boundary condition settings, the following assumptions should also be made:

(1) Proppants are assumed to be spherical or regular geometric bodies, and the influence of shape irregularity on transport is ignored. This assumption allows the micro-scale force interactions to be analyzed in a controlled manner and has been widely adopted in CFD-DEM studies of proppant transport. (2) The density and particle size of proppants are assumed to be constant, and the mixing effect during graded injection is ignored. (3) Proppants are assumed not to break during transport, and only sedimentation, collision, and slip are considered, which is reasonable for short transport times and moderate stress conditions. (4) The viscosity of the fracturing fluid is set to a constant value or dynamically adjusted according to the displacement. (5) The filtration in the fracture is ignored. (6) Temperature changes in the fracture are ignored.

3. Results and discussion

3.1. Flow patterns and their development

The same boundary conditions in planar and rough fractures are set to investigate the flow regimes in rough fractures. The relative parameters are in Table 1. Fig. 3 includes the proppant placement and flow field at the same dimensionless time, defined as the ratio of the injected volume of a fluid to the fracture space available. The equation is as follows:

Table 1
Parameters in simulation.

Case#	Injection velocity, m/s	Injection concentration	Fractal dimension	Inclination angle	Dimensionless viscosity
1	0.15	0.03	2.3	0°	1
2	0.15	0.03	2	0°	1
3	0.10	0.03	2.3	0°	1
4	0.20	0.03	2.3	0°	1
5	0.15	0.03	2.3	30°	1
6	0.15	0.03	2.3	45°	1
7	0.15	0.03	2.3	60°	1
8	0.15	0.03	2.3	90°	1
9	0.15	0.03	2.3	30°	3
10	0.15	0.03	2.3	45°	6
11	0.15	0.03	2.3	90°	9

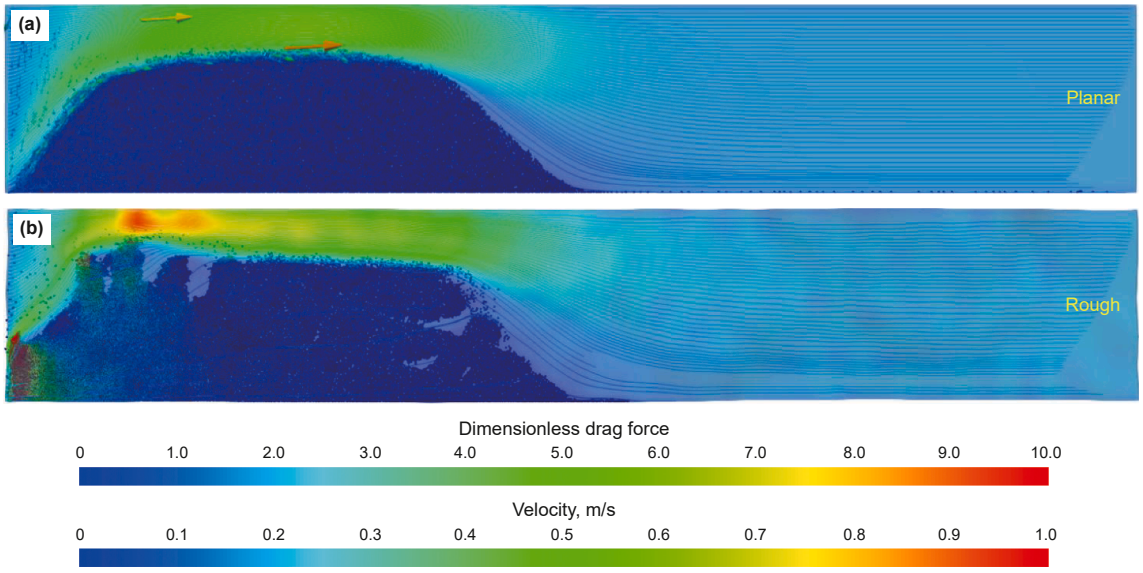


Fig. 3. Snapshots of the field, proppant placement, and dimensionless drag force at the same dimensionless time with different type fractures: (**a**) planar fracture and (**b**) rough fracture.

$$T = \frac{tvS}{V} \tag{8}$$

where T represents the dimensionless time, t is the actual injection time, v is the injection velocity, S is the average cross-sectional area of the fracture, and V is the volume of the fracture. It is commonly used in multiphase flow studies and previous works (An et al., 2020; Song et al., 2024; Zhou et al., 2024). Fig. 3 shows continuous dunes in the planar fracture, discontinuous dunes in the rough fracture. In planar fractures, proppant transport is dominated by relatively uniform flow fields, leading to continuous dune structures with gradual spatial variation. In contrast, the presence of rough fracture disrupts the local flow field and induces strong spatial heterogeneity, resulting in segmented and discontinuous blocky dunes. This structural difference is accompanied by distinct force balance characteristics, where particle–particle interactions and localized fluid–particle forces play a more prominent role in rough fractures. The comparison highlights that proppant transport mechanisms identified in smooth fractures cannot be directly extended to rough fracture conditions. In particular, the emergence of blocky dunes introduces different flow regime transition behaviors and transport efficiency characteristics. Blocky dunes contain abundant internal voids, which constitute their typical feature. The blocky dune generation and the influence factors have been observed and studied in previous works (Song et al., 2024; Yang et al., 2024). In this work, the changes in the flow regime have been investigated.

From Fig. 3, discontinuous blocky dunes give rise to a fragmented fluidized layer and eject more particles into the flow field. It is necessary to analyze the force characteristics on a microscopic scale to understand the flow regimes of continuous and blocky dune development processes. Drag force is a core parameter describing fluid and particles momentum and energy transfer. For a single particle, the drag force formula is expressed as follows (Li et al., 2011):

$$\boldsymbol{f}_{\mathrm{drag},i} = \frac{1}{8}\rho_{\mathrm{f}} C_{\mathrm{D}} \pi d_{\mathrm{eq}}^2 \left|\boldsymbol{v}_{\mathrm{f}} - \boldsymbol{v}_{\mathrm{s}_i}\right| \left(\boldsymbol{v}_{\mathrm{f}} - \boldsymbol{v}_{\mathrm{s}_i}\right) \tag{9}$$

where $\boldsymbol{f}_{\mathrm{drag},i}$ is the drag force on particle i, ρ_{f} is the density of fluid, C_{D} is the drag coefficient, d_{eq} is the mean particle diameter. $\boldsymbol{v}_{\mathrm{s}_i}$ is the velocity of particle i, $\boldsymbol{v}_{\mathrm{f}}$ is the velocity of fluid. At the same time, these parameters are all constant except the velocity of particles and fluid. Thus, from the formula, $\boldsymbol{f}_{\mathrm{drag},i}$ depends on the value of the relative velocity between the velocity of particle and the velocity of fluid surrounding the particle. For the expanded application, dimensionless drag force Π_1 and dimensionless particle–particle force Π_2 are used and refer to Kuang's and Zhou's works (Kuang et al., 2009; Zhou et al., 2020) and is expressed as follows:

$$\Pi_1 = \frac{\left| \frac{1}{\Delta t}\sum_{\Delta t}\left[\frac{1}{V_{\text{section}}}\left(\sum_{i=1}^{N_{\text{p.section}}} \boldsymbol{f}_{\text{drag},i} \right) \right] \right|}{\frac{1}{\Delta t}\sum_{\Delta t}\left[\frac{1}{V_{\text{section}}}\left(\sum_{i=1}^{N_{\text{p.section}}} m_i g \right) \right]} \tag{10}$$

$$\Pi_2 = \frac{\frac{1}{\Delta t}\sum_{\Delta t}\left\{ \frac{1}{V_{\text{section}}}\left(\sum_{i=1}^{N_{\text{p.section}}} \left(\sum_{j=1}^{k_i} \left| \boldsymbol{f}_{\text{cn},ij} + \boldsymbol{f}_{\text{ct},ij} \right| \right) \right) \right\}}{\frac{1}{\Delta t}\sum_{\Delta t}\left[\frac{1}{V_{\text{section}}}\left(\sum_{i=1}^{N_{\text{p.section}}} m_i g \right) \right]} \tag{11}$$

where V_{section} is the volume of the cells in the fracture section, $N_{\text{p.section}}$ is the number of particles in the fracture section. Where $\boldsymbol{f}_{\text{cn},ij}$ and $\boldsymbol{f}_{\text{ct},ij}$ denote the normal and tangential contact forces, respectively, acting between particle i and its neighboring particle or wall j. The normal contact force $\boldsymbol{f}_{\text{cn},ij}$ represents the compressive interaction arising from particle–particle or particle–wall collisions, while the tangential contact force $\boldsymbol{f}_{\text{ct},ij}$ accounts for frictional and shear interactions along the contact surface. These contact force components collectively characterize the contribution of inter-particle and particle–wall interactions to the overall force balance. These two types of forces can be expressed relative to particle gravity to facilitate their comparison with particle gravity.

Fig. 4 exhibits the dimensionless drag force Π_1 versus dimensionless time curves at planar and rough fractures. They all experience two stages, an initial decrease followed by an increase. In the first period, the generation of drag force results from sediment of particles by gravity. Then, as the number of the settling particles, which are surrounded by relatively static fluid and have little drag force, increases, dimensionless drag force increases because it is a mean value. This is due to the combination effect of all the particles being static and suspended. When the single hill is shaped, the interaction area increases. It makes the more fluidized layer particles receive the drag force. Not only that, but the developing stages of the dune also shape the uneven and distorted channel. It raises the resistance of the flow. A narrow channel increases fluid velocity, which causes drag force to grow further. The identification of different flow regimes is based on the variation trend and slope change of the Π_1 curve rather than its absolute magnitude. Specifically, a negative slope of Π_1 indicates a settlement-dominant stage, whereas the transition to a scour-dominant stage is marked by a clear turning point where Π_1 reaches a local minimum and subsequently increases. Fig. 4 illustrates some feature points and corresponding flow regimes (flow pattern with dimensionless drag force and the streamlines). Based on the above analysis, the flow pattern can be divided into two periods: one is the settlement-dominant stage (Fig. 4(a) from I to II, and (b) from I to II), and the other is the scour-dominant stage (Fig. 4(a) after II and including III, (b) after II and including II, IV). The flow pattern of II in Fig. 4 is a critical status.

Under identical injection conditions, the difference between planar and rough fractures is that dunes in rough fractures increase periodically during the scour-dominant stage, with a growth rate significantly higher than that in planar fractures. Due to their blocky shape, these dunes have sharp edges, making it challenging for the fluidized layer to be tangent to their surfaces. Furthermore, the blocky dunes form narrow channels between them. Both reasons cause the velocity difference to be longer, increasing the dimensionless drag force.

3.2. Effect of injection velocity

Injection velocity is crucial in proppant transport as it provides the main transport power. Three injection velocities (0.1, 0.15, and 0.2 m/s), corresponding to Case 1, Case 3 and Case 4 in Table 1, are adopted to investigate their effects on blocky dune features within rough fractures. Fig. 5 describes proppant placement under different injection velocities. An upward trend can be seen in DPBL with increasing injection velocity while the DPBH decreases. The reason is that a larger injection velocity provides more energy to transport the proppant further. At the same time, as shown in the area enclosed by the red dotted line, the injection velocity of 0.2 m/s exerts a significant influence on the dunes near the fracture inlet. Under this condition, the fracture inlet fails to obtain sufficient proppant support, leading to reduced fracture conductivity.

Fig. 6(a) exhibits the dimensionless drag force Π_1 versus time curves at different injection velocities. It demonstrates that the changing tendency is the same. The lowest value is larger when the velocity increases. Under high-velocity fluid, static particles have a larger velocity difference from the surrounding fluid, which makes the dimensionless drag force larger during the settlement-dominant stage. During the scour-dominant stage, the value of the lowest velocity increases the drag force. This is because the DPBH is higher in the lower injection velocity case, which narrows the channel and increases the contact area. The sharp turning point at the dimensionless time value is around 6, the plugging generated at that time. Then it suffers from collapse soon. Details of the relevant studies and explanation are in previous works (Yang et al., 2024).

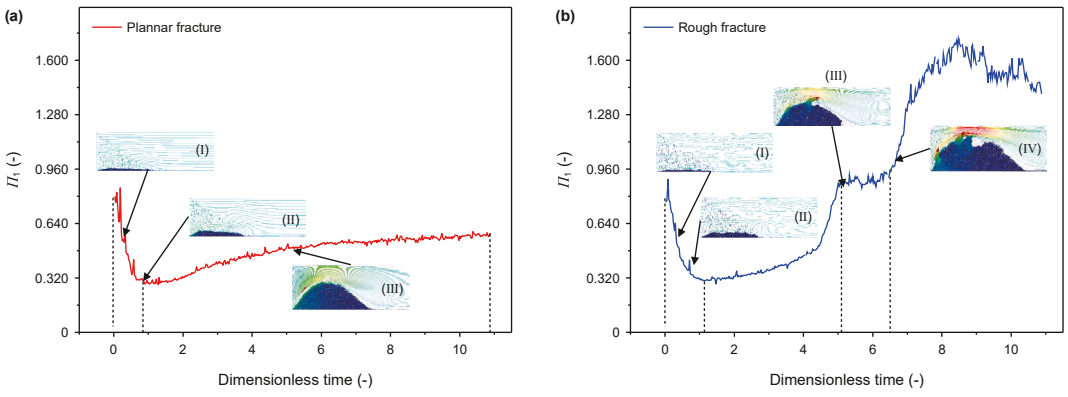


Fig. 4. Dimensionless drag force Π_1 versus dimensionless time curves, drag force phase, and corresponding streamlines at different stages: (**a**) planar fracture; (**b**) rough fracture.

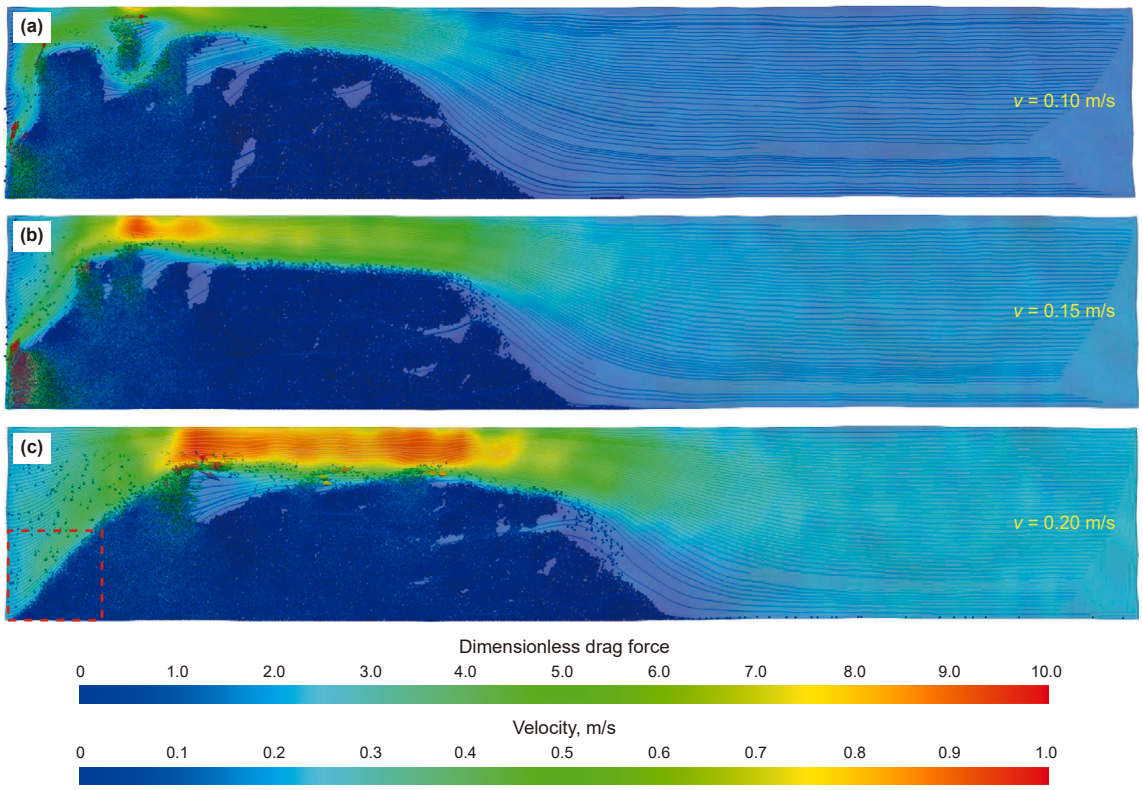


Fig. 5. Snapshots of the field, proppant placement, and dimensionless drag force at the same dimensionless time with different injection velocities: (**a**) $v = 0.1$ m/s; (**b**) $v = 0.15$ m/s; (**c**) $v = 0.2$ m/s.

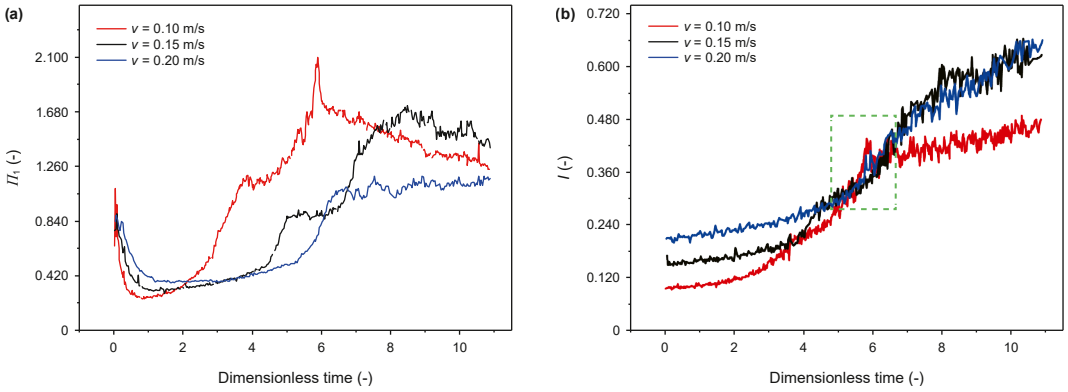


Fig. 6. Dimensionless drag force Π_1 (**a**) and dimensionless pressure drop I (**b**) versus time curves at different injection velocities.

Fig. 6(b) demonstrates the changing process of dimensionless pressure drop curves' response to different injection velocities. Dimensionless pressure drop refers to Zhou et al.'s work (Zhou et al., 2020) and Ravelet et al.'s work (Ravelet et al., 2013). It is applied in hydraulic conveying work (Zhou et al., 2019, 2020), and it is defined as:

$$I(m/m) = \frac{\Delta P}{\rho_f g L} \tag{12}$$

where I is the dimensionless pressure drop. Since ρ_f, g, L are the same, pressure drop ΔP is a decisive factor. ΔP is calculated using the Darcy-Weisbach's equation to evaluate the fluid phase pressure drop (Li et al., 2011) and is expressed as:

$$\Delta P_f = 2f\frac{L\rho_f \boldsymbol{u}^2}{D} \tag{13}$$

$$D = \frac{4A}{X} \tag{14}$$

$$\frac{1}{f^{1/2}} = \frac{4}{(n')^{0.75}} \lg\left[Re_{MR} f^{\left(1-\frac{n'}{2}\right)}\right] - \frac{0.4}{(n')^{1.2}} \tag{15}$$

$$Re_{MR} = \frac{\rho u^{2-n'} D}{K \cdot (3n'+1)/(4n')} \tag{16}$$

where L is length of fracture model, D is inner diameter of pipe or the equivalent diameter of fracture model, A and X are the cross-section area and wetted perimeter of fracture model, f is friction coefficient of Fanning, Re_{MR} is Reynolds of Metzner-Reed, K is consistency coefficient of power-law fluids, n' is rheological index of power-law fluids. For Newtonian fluid, n' value is 1. From the formula, the pressure drop depends on different flow regime and the changing velocity.

Comparing the previous works about continuous dunes (Zhou et al., 2024), the pressure drop curves of blocky dunes are different from the continuous ones. Specifically, it has no obvious stages like exponential mode and linear mode, and more fluctuating stages were generated during the whole developing period. Overall, a larger injection velocity causes a larger pressure drop. This is because the friction between high-velocity fluid and wall/dunes increases. This is why before dimensionless time is 4, the high-velocity has a larger pressure drop. It is the same as the planar fracture in previous works (Zhou et al., 2024). The difference in blocky dune is in the scour-dominant stage. It is because, as mentioned before, there will be plugging in rough fractures. It is also consistent with the dimensionless drag force curves in this regard. This phenomenon is also observed in Huang et al.'s work (Huang et al., 2024). The pressure drop sharply grows with that injection velocity of 0.1 m/s and exceeds higher injection velocity cases. This indicates that lower injection velocity not only reduces the placement distance but also tends to induce plugging within blocky dunes. As shown in Fig. 7, the pressure drops under the three injection velocities tend to converge within the dimensionless time range of 5–7. Because higher injection velocity causes lower DPBH, the flow resistance can decline to a certain extent. Injection velocity and dune height are the two factors that influence the pressure drop. Finally, they restrict each other until equilibrium is reached.

Fig. 7 describes the dimensionless particle–particle force Π_2 versus τ curves at different injection velocities. The overall trend increases, but in the dune development stage (corresponding scour-dominant stage), high-velocity has lower Π_2. It can illustrate the flow regimes at different injection velocities with Π_2. In this case, Π_2 stands for the particles' chance of collision and strength. Lower Π_2 demonstrates more energy works on the dune inert than transport. It can also illustrate that the number of suspended and fluidized layers is larger relatively during the dune development stage, which implies the potential transport ability. This flow regime is favorable for proppant transport, as more injected energy is consumed in particle mobilization rather than being dissipated through particle–particle contacts. Therefore, higher injection velocity enhances proppant transport efficiency primarily by reducing inter-particle interaction forces and promoting particle suspension.

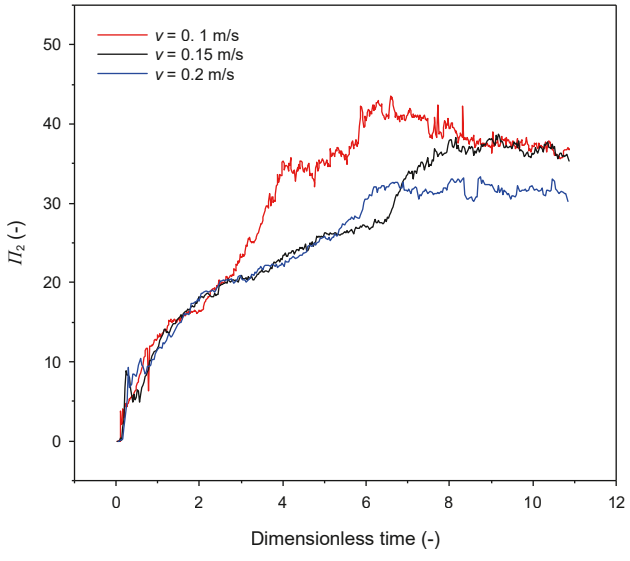


Fig. 7. Dimensionless particle–particle force Π_2 versus dimensionless time curves at different injection velocities.

3.3. Effect of fracture inclination angle

From a mechanistic perspective, fracture inclination angle directly alters the relative contributions of gravitational forces acting parallel and normal to the fracture plane. As the inclination angle increases, the component of gravity parallel to the fracture enhances particle sliding and downslope transport, whereas the normal component governs particle settling and contact force development. This redistribution of gravitational effects modifies the force balance controlling blocky dune stability, resulting in observable variations in dune morphology, migration behavior, and flow regime characteristics. To systematically investigate the influence of fracture inclination on proppant placement and flow regimes, five representative inclination cases are considered in the simulations. Fracture inclination is implemented by varying the direction of the gravitational acceleration vector. The selected inclination angles are 0° (parallel to gravity), 30°, 45°, 60°, and 90° (perpendicular to gravity), as summarized in Case 1, Case 5, Case 6, Case 7 and Case 8 of Table 1.

Fig. 8 indicates the flow field, proppant transport, and dimensionless drag force. It can be found that increasing inclination angle can expand the DPBL and diminish the mean DPBH. This is because inclination angle increasing is equivalent to increasing the sediment area in the flat layer stage (settlement-dominant stage) (Zhou et al., 2024). During the dune development stage, an incline fracture has a shortened settlement distance from the highest point in the fracture so that the dune can develop earlier. That is why the proppant can be transported more quickly and have a wider placement area. When the fracture is vertical, its initial sediment area is only the bottom of the fracture. It is noticeable that horizontal fracture (90°) has good transport ability and cannot form a sediment layer.

Not only that, but the geometric characteristics of dunes directly narrow the flow channels and alter their internal flow field distribution. Due to the fluid velocity being smaller, the dimensionless drag force in different inclination fractures also follows the rules above. The overall trend is the same as the one in the previous analysis. During the settlement-dominant stage, the changing trend roughly overlaps. As the inclination angle is 90°, there is no integrated settlement stage. After it is not referred to, during the scour-dominant stage, with the inclination climbing, the Π_1 drops, and the curve shape are similar. Fig. 9(a) shows the distribution and direction of the dimensionless drag force acting on particles. Two main places contribute to the large drag force a lot. One is the placement at the entrance, which does not exist in high-inclination fractures. The other is the obtrusive part, a dotted line mark in yellow, which is the blocky characteristic. It can change the fluid field and flow direction, dissipating some energy by exerting greater drag force. This blocky feature disappears when the inclination ascends. The inclination continues to grow, becoming more similar to planar fracture. A lower dimensionless

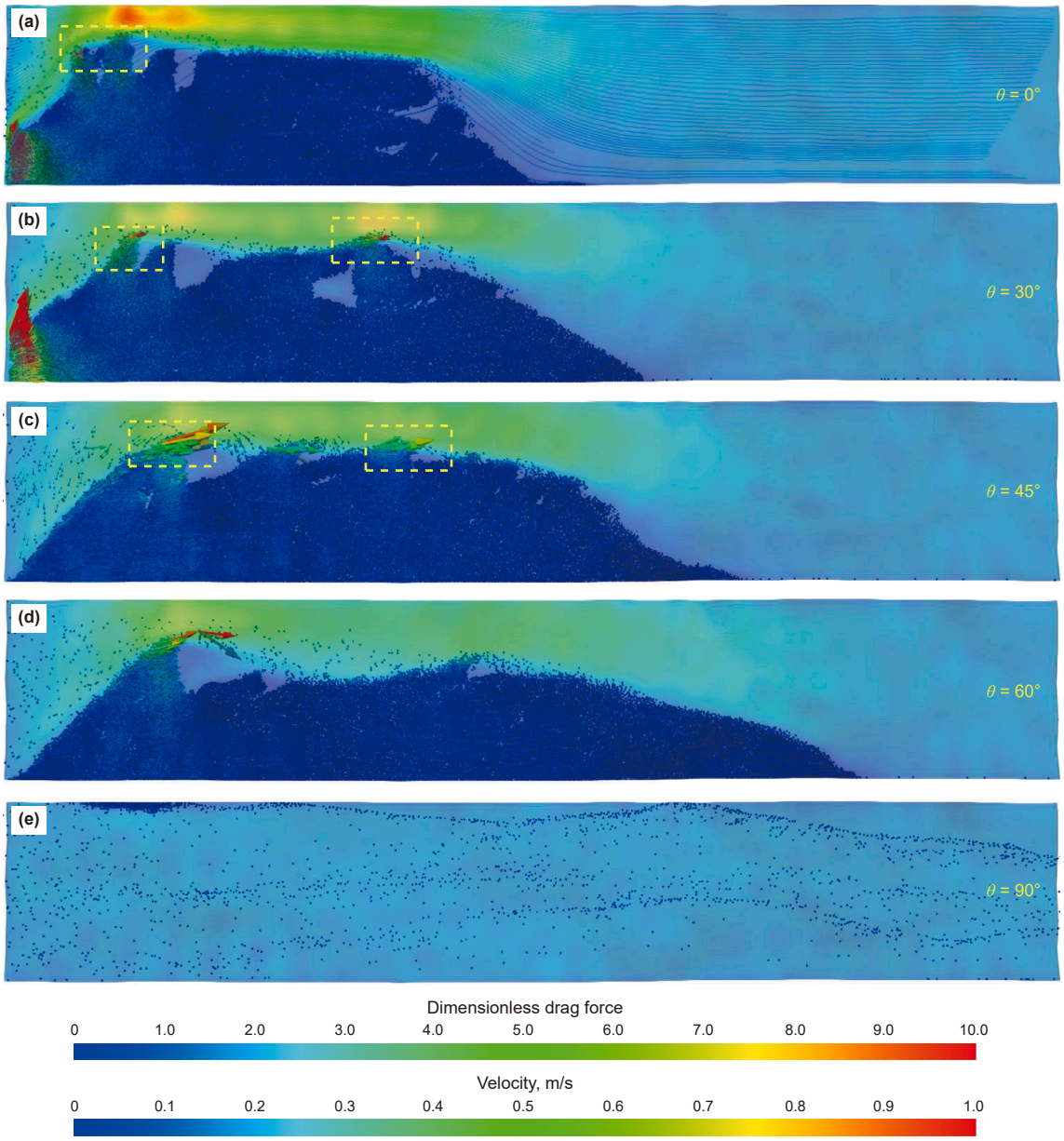


Fig. 8. Snapshots of the flow field, proppant transport, and dimensionless drag force at the same dimensionless time with different inclination angles: (**a**) 0°; (**b**) 30°; (**c**) 45°; (**d**) 60°; (**e**) 90°.

drag force represents less velocity difference, which can directly influence energy loss and induce a lower pressure drop.

As shown in Fig. 9(b), the dimensionless pressure drop varies with fracture inclination. A smaller inclination angle is associated with a lower dune height, which enlarges the effective flow channel and reduces flow resistance. In addition, under lower inclination angle conditions, the reduced fluid–particle drag leads to less energy dissipation during proppant transport, allowing more injection energy to be preserved in the fluid phase. As a result, fractures with smaller inclination angles exhibit a lower dimensionless pressure drop, indicating improved flow capacity and fracture conductivity.

Dimensionless particle–particle force Π_2 is shown in Fig. 10 to understand the placement with different inclination angles. Each particle–particle curve line experiences an increase to different extents except for horizontal fracture. More inclination results in less particle–particle force. This shows particles in incline fractures have less contact and work together. It is a benefit to the transport. That's why the high-inclination fracture has quicker transport and broader area. Therefore, it is necessary to decrease the chance of contact to have good transport ability. The most efficient transport pattern is like horizontal fracture, which uses all fluid energy to move further in the fracture.

3.4. Effect of the fluid viscosity

Hydraulic fracturing fluid viscosity is a key parameter controlling proppant transport behavior. Fig. 11 illustrates the flow field and proppant placement patterns obtained using fluids with different viscosities (see Case 1, Case 9, Case 10 and Case 11 in Table 1) at the same dimensionless time. Herein, the dimensionless viscosity is realized by relative viscosity, which is defined as the ratio of the fluid viscosity to the reference viscosity of water, ensuring the consistency of parameter normalization in the

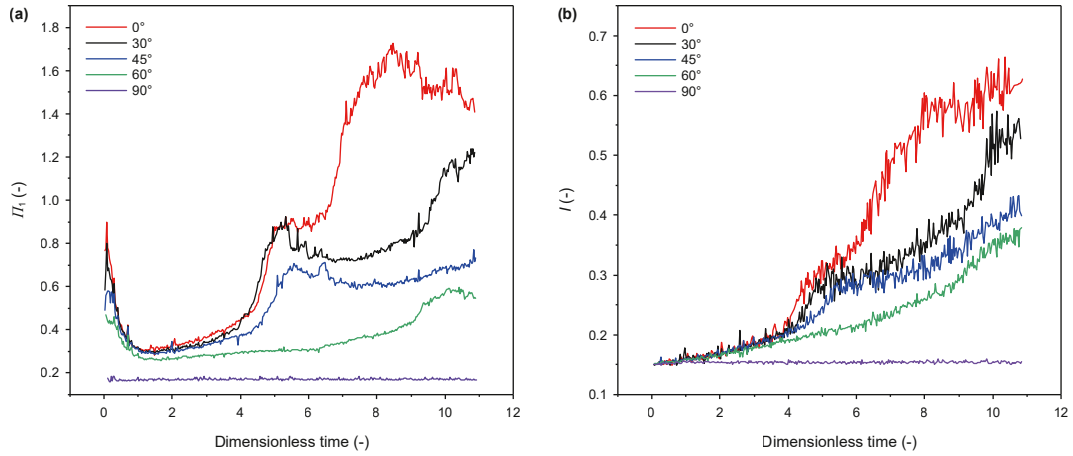


Fig. 9. Dimensionless drag force Π_1 (**a**) and dimensionless pressure drop I (**b**) versus dimensionless time curves at different inclination angles.

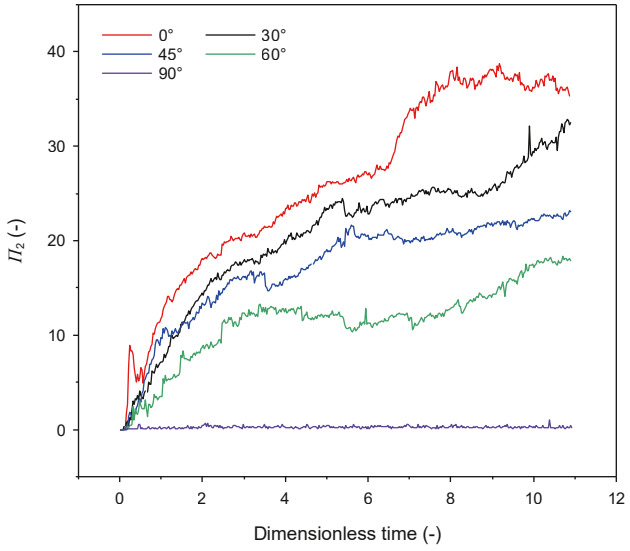


Fig. 10. Dimensionless particle–particle force Π_2 versus dimensionless time curves at different inclination angles.

simulation. As fluid viscosity increases, the proppant transport distance is extended, while the overall placement height of the proppant dunes decreases, indicating a redistribution of particles along the fracture. The increased viscosity significantly modifies the local flow field structure. As highlighted by the dotted regions and the enlarged views on the right side of Fig. 11, particles entrained in high-velocity flow regions experience highly fluctuating fluid–particle interaction forces. These fluctuations lead to disordered drag force directions, which promote particle rearrangement and contribute to the observed changes in dune morphology and transport characteristics. As fluid viscosity varies, a clear trend in proppant dune morphology can be identified. At lower viscosity values, the settling velocity of proppants is relatively high and the fluid–particle interaction force is comparatively weak, allowing particles to deposit more rapidly and form relatively stable blocky dune structures. As fluid viscosity increases, the enhanced fluid–particle interaction intensifies the disturbance exerted by the flowing fluid on the dune surface, leading to increased particle rearrangement and a more loosened dune structure. Consequently, higher viscosity conditions tend to promote dune deformation and dispersion rather than stabilization.

Fig. 12(a) is a dimensionless drag force Π_1 curve at different dimensionless times within different fluid viscosities. Overall, the highly viscous fluid corresponds to the drag force being bigger. It is not difficult to understand the curve changes over a later time. However, the strange point is that the changing trend for the time before 3 is not obvious with the large viscosity. Only the case with $\mu_D = 9$ exhibits a monotonically increasing trend. Accordingly, the flow regime within a specific time interval needs to be analyzed. Fig. 12(a) presents the streamlines, proppant distribution, and dimensionless drag force acting on proppant particles at the dimensionless time $\tau = 3$. At this time, all cases are in the flat layer stage (settlement-dominant stage). The viscous drag region, the suspended particle area, increases when the fluid viscosity increases. It demonstrates a weaker settlement trend, so the distance is longer. From the previous studies, this characteristic parameter of the flat layer distance is a property of a specific boundary condition (Zhou et al., 2024). As illustrated in Fig. 13, the abnormal variations can be attributed to two factors. On the one hand, suspended particles dominated by drag force account for a large proportion of total particles. On the other hand, erosion induced by high-viscosity fluids remodels the bed into distinct dune morphologies, where abundant fragmented blocky dunes emerge especially under the corresponding flow condition. Each abrupt little dune has resistance to the fluid; at the same time, when the streamline passes through, it cannot smoothly cut into the little dune. It can generate a strong velocity difference and result in greater drag force.

Fig. 14 exhibits the diagram of particles subjected to dimensionless drag force direction under different conditions in a part of the blocky dune. There are four types of drag force directions. Particles I are suspended particles in front of the dune. The drag force direction is opposite to the settling direction. Particles III are the back of the dune with little disturbing. They are similar to particles I. Particles II are in a fluidized layer with a continuous dune location. They have an approximately consistent direction with the flow field direction there. At the same time, it is also tangent to the fluidized dune. Unlike the others, particles IV are in blocky dune cutting edge, which has a larger friction. The fluid velocity difference between the fluid and the particles depends on the flow field direction. Therefore, the drag force direction is consistent with the flow field direction but hard to tangent to the dune surface. All four drag force directions coexist within complex blocky dune structures.

Fig. 12(b) is dimensionless pressure drop curves at different fluid viscosities within different dimensionless times. Generally

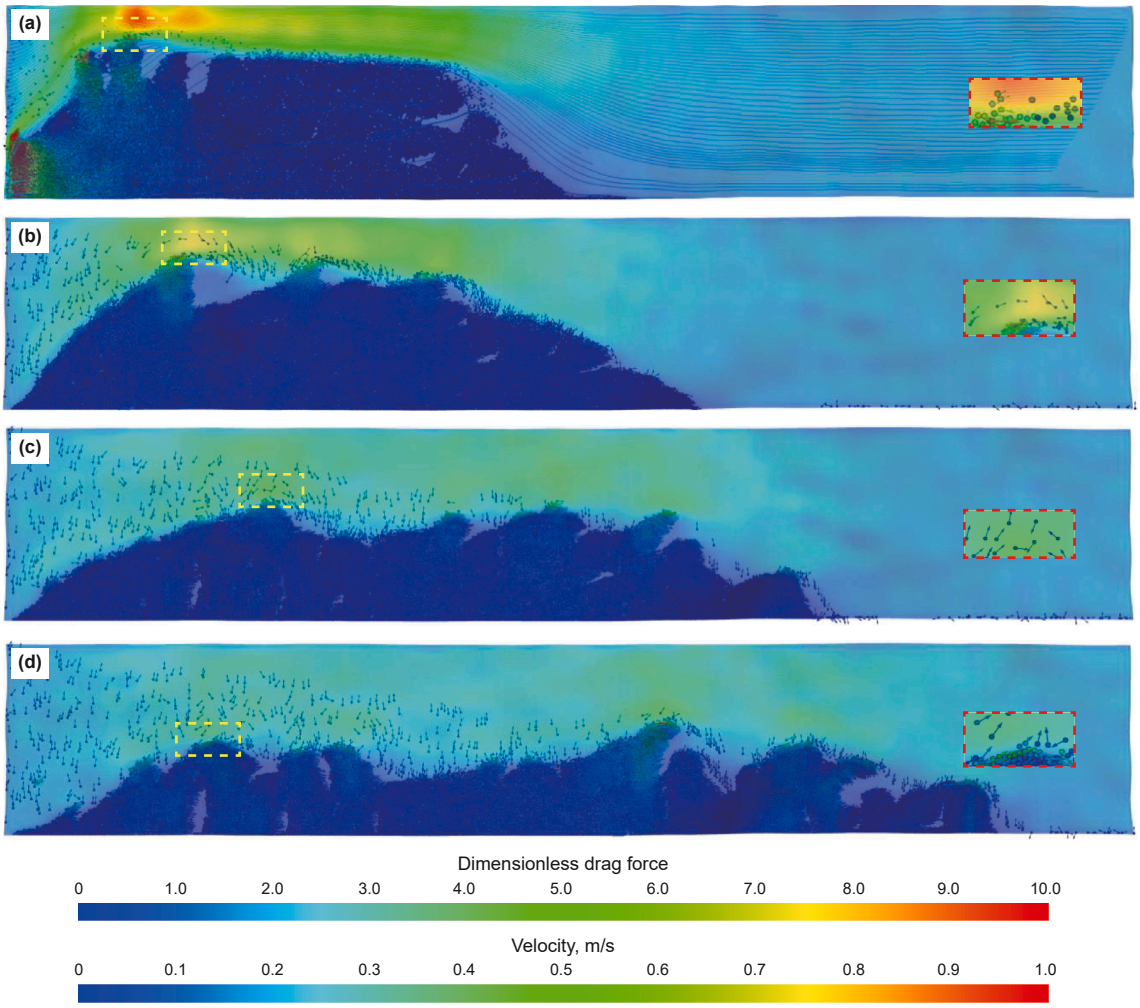


Fig. 11. Snapshots of the flow field, proppant transport, and dimensionless drag force at the same dimensionless time with different dimensionless viscosities: (**a**) $\mu_D = 1$; (**b**) $\mu_D = 3$; (**c**) $\mu_D = 6$; (**d**) $\mu_D = 9$.

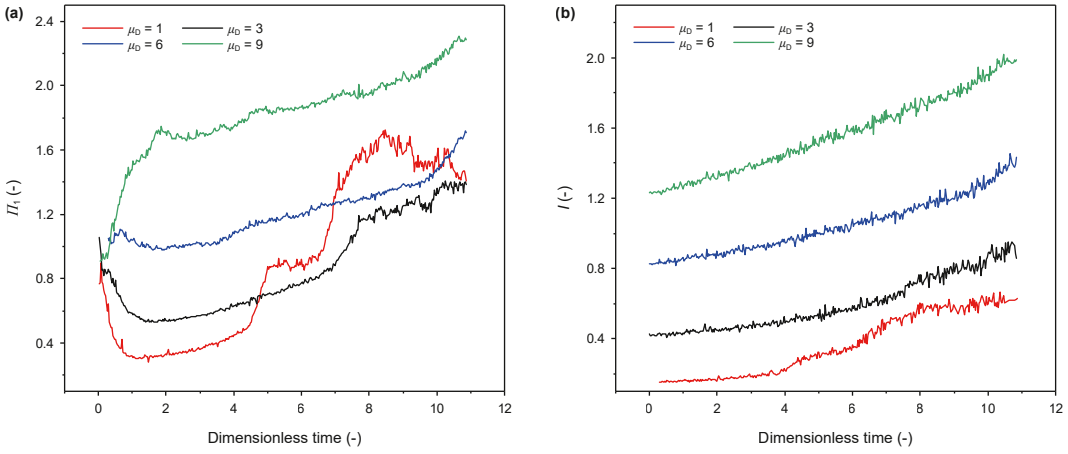


Fig. 12. Dimensionless drag force Π_1 (**a**) and dimensionless pressure drop I (**b**) versus dimensionless time curves at different fluid viscosities.

speaking, fluids with high viscosity have larger pressure drops and smaller fluctuations and are smoother than fluids with low viscosity. The high viscosity eliminates the possibility of sand plugging and ensures a stable increase in pressure drop. Although from the placement, the highly viscous fluid has strong erosion on the dune at the entrance of the fracture, which will reduce the greater resistance of the fluid, the longer distance dune and more contact area still strengthen the resistance. Besides, the pressure drop is due to the friction between the fluid and the dune. In highly viscous fluid, the smaller overall flow field velocity indicates the

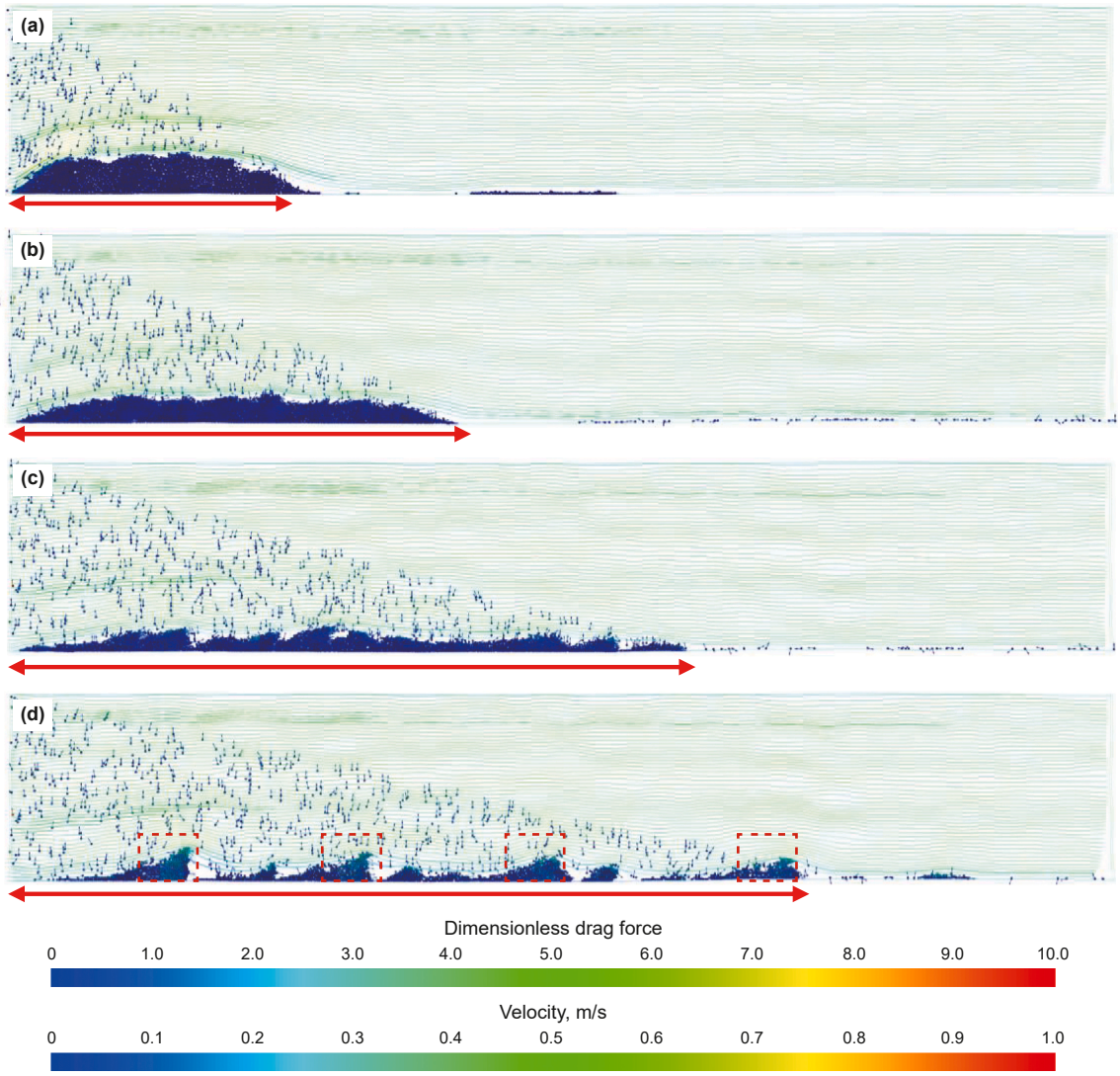


Fig. 13. Snapshots of the streamlines, proppant transport, and dimensionless drag force at the same dimensionless time with different dimensionless viscosities: (**a**) $\mu_D = 1$; (**b**) $\mu_D = 3$; (**c**) $\mu_D = 6$; (**d**) $\mu_D = 9$.

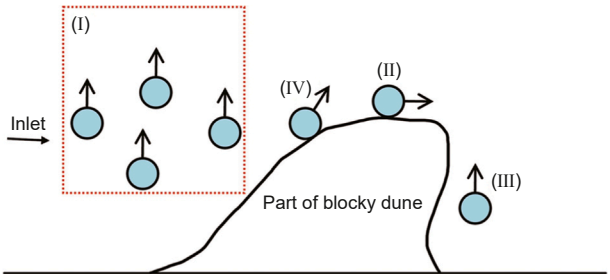


Fig. 14. Schematic diagram of particles subjected to dimensionless drag force direction under different conditions in a part of the blocky dune. (I) Suspended particles; (II) fluidized layer particles; (III) backflowing particles; (IV) particles in blocky dune cutting edge.

consumption of more injection energy, which is lost in transporting proppant and converted into pressure drop. This higher consumption is relative to the high viscosity fluid and rough fractures wall to a large extent. Fortunately, this energy transfer causes the dunes to move further, instead of being severely lost at the entrance because of the high viscosity fluid sweeping characteristic. Finally, a few reasons appear in the high viscosity fluid, a high Reynolds number, which will produce more eddy disturbances, thereby increasing energy loss, especially in systems with unstable flow fields such as rough fractures.

Fig. 15 is a dimensionless particle–particle force curve with dimensionless time at different injection velocities. Apart from the special properties caused by the blocky dune with a fluid viscosity of 1, the overall dimensionless particle–particle force varying trend maintains a monotone trend. The viscosity of the proppant-carrying fluid has a positive correlation with the magnitude of the hydrodynamic force acting on proppant particles. Based on the above analysis, a better transport case should have little particle–particle force, which reduces intersections, constraints, and collisions among particles, thereby increasing the chance of forward transport. But the result is an adverse interpretation here. The long-distance transport of particles is not attributed to weakened particle–particle bonding, but to the reduced particle settling velocity and prolonged settling time in high-viscosity fluids. There are more particles in the suspended layer, and more energy is transferred by the fluid, resulting in less resistance from

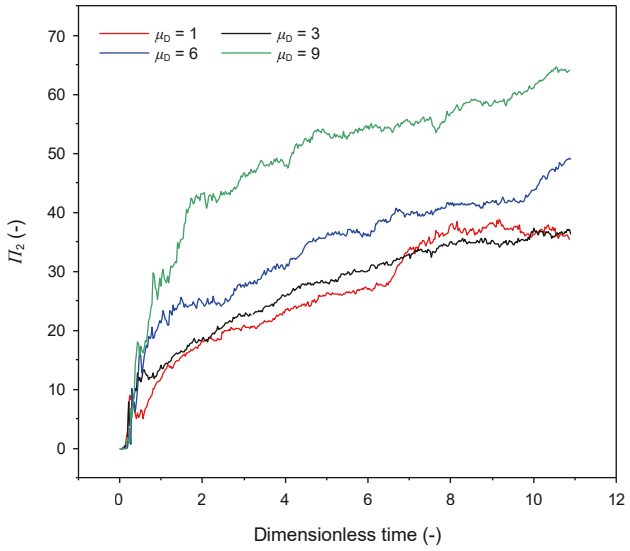


Fig. 15. Dimensionless particle–particle force Π_2 versus dimensionless time curves at different fluid viscosities.

the bed. And the particles can move further in the suspended layer. However, simultaneously, due to the huge liquid exerting pressure on the bed, the dune must have enough force to balance it. Therefore, the greater the viscosity, the closer the particles are to each other and the greater the force.

From the above study, depending on micro-internal mechanisms with dimensionless drag force, pressure drop and particle–particle force, there are 2 internal factors that influence the efficiency of proppant transport, settlement time and particle–particle force. For cases with varying injection velocities, enhanced proppant transport is achieved with nearly constant settling time and lower particle–particle force compared with the reference case. It means that the strategy of injection velocity enhances the transport by reducing the particle–particle force. For the cases with different fluid viscosities, it has increasing particle–particle force and settlement time, but is still with a promoting effect. It means it can improve the proppant transport by increasing settlement time. Similarly, the cases with different fracture inclination angles decrease the settlement time and increase the particle–particle force. The net promoting effect arises because the benefit of reduced inter-particle force outweighs the inhibitory impact of shortened settling time. The corresponding function table is shown in Table 2.

3.5. Multi-factor analysis of proppant placement by means of the orthogonal test method

Orthogonal tests are based on statistics and the principle of orthogonality. It can reduce the number of trials and resource usage by choosing typical components and levels from full evaluation locations. It is a fast and economical experimental design method and an important solution for studying multi-factor and multi-level problems. The physical mechanisms underlying the orthogonal test results can be interpreted by linking the dominant factors to the micro-scale force analysis discussed in Sections 3.1–3.4. Injection velocity primarily affects proppant transport by regulating the fluid–particle relative velocity, thereby directly controlling the dimensionless drag force Π_1 and the particle suspension capability during the scour-dominant stage. Proppant concentration mainly influences the particle–particle interaction force Π_2 by altering collision frequency and mechanical constraints within the proppant bed, which governs dune stability and settling behavior. In contrast, fracture roughness modifies local flow channels and contact conditions, affecting both Π_1 and Π_2 by enhancing velocity gradients and force transmission heterogeneity. Therefore, the factor importance ranking obtained from the orthogonal analysis is physically consistent with the force-based mechanisms identified at the particle scale, providing a coherent interpretation of the macroscopic sensitivity results.

The above study illustrates the micro-internal mechanisms of multiple factors including injection velocity, fracture inclination angle and fluid viscosity. For analyzing the effect on proppant placement with these factors, the orthogonal test method was used to compare the extent of influence and find the relatively more optimized setting. After simulating the comprehensive effects of viscosity and fracture inclination angle, it was found that it can shape a suspension transport. This can verify the above study that increasing fracture inclination angle improves the transport effect through decreasing particle–particle force. However, it cannot be used for discussing the effect on DPBH and DPBL owing to the fact that the suspension transport cannot generate dune. It means that the orthogonal test including fracture inclination is not the scope of the consideration. Therefore, the W_d was selected to analyze multi-factor analysis of proppant placement. Meanwhile, a wider range of W_d can capture the effects of more fracture types.

In orthogonal tests, an orthogonal list is commonly used to analyze the measured results, which is usually expressed as $Ln(t^c)$ (where L represents the orthogonal list number, n represents the number of tests, t represents the number of levels of factors, and c represents the number of columns or the possible maximum number of factors). To meet the requirements of any orthogonal list, each factor corresponds to 3 levels, which ensures that the proppant placement is optimal when any other factor remains unchanged. Therefore, a certain number of tests need to be carried out in total (which can be calculated according to the orthogonal table). The $L9\left(3^3\right)$ orthogonal level list and the corresponding orthogonal list are shown in Tables 3 and 4 respectively.

Table 3
$L9\left(3^3\right)$ orthogonal level list.

	Incline angle (A)	Injection velocity (B), m/s	W_d (C)
Level 1	0°	0.1	0.3
Level 2	30°	0.15	0.4
Level 3	60°	0.2	0.6

Table 2
Action characteristics of proppant transport influencing factors: settling time and particle–particle force.

Influential factors	Settlement time	Particle–particle force	Effect on proppant transport (promoting or slowing)
Injection velocity	–	↓	+
Fracture inclination angle	↓	↓	+
Fluid viscosity	↑	↑	+

Table 4
$L9\left(3^3\right)$ orthogonal list.

Trial No.	A	B	C
1	1	1	1
2	1	2	3
3	1	3	2
4	2	1	3
5	2	2	2
6	2	3	1
7	3	1	2
8	3	2	1
9	3	3	3

The range analysis method is typically used to analyze orthogonal test results. The range is denoted by R_j, which is the difference between the largest and minimum average values under the level of factors in the j column, and the following is the corresponding computing formula:

$$R_j = \max\left(k_{1j}, k_{2j}, \ldots, k_{ij}\right) - \min\left(k_{1j}, k_{2j}, \ldots, k_{ij}\right) \quad (17)$$

where, k_{ij} represents the total of corresponding test data of level i of the factors in the j column.

The larger the R_j, the more significantly the variation of the factor impacts the measured results; that is, this factor is more sensitive to the measured results. Hence, the significance factors of the testing level may be determined using the measured results.

DPBL and DPBH are used to evaluate the effect of these factors on proppant transport, where K_i represents the total of all DPBL and DPBH under level i of a certain factor and k_i represents the average of all DPBL and DPBH under level i of a certain factor, whose optimal level is defined as the level corresponding to the factor (level = the maximum of k_i for each column).

Analysis results of ranges in Tables 5 and 6 reflect the optimal combination (A3B3C1) for DPBL and A2B1C3 for DPBH. The data shows that for DPBL, the most significant impact is the incline angle and the effect of others under the setting of this range are the same. For DPBH, the most significant impact is injection velocity, which can decrease the height of the dune greatly. The next sorting is W_d and incline angle.

Table 5
Analysis of ranges of orthogonal results (DPBL).

Trial No.	A	B	C	DPBL
1	1	1	1	0.4778
2	1	2	3	0.2793
3	1	3	2	0.5391
4	2	1	3	0.2559
5	2	2	2	0.5496
6	2	3	1	0.8321
7	3	1	2	0.6069
8	3	2	1	1.0000
9	3	3	3	0.8620
K1	1.296206618	1.340597256	2.309927361	
K2	1.637610977	1.82889427	1.695722357	
K3	2.468926554	2.233252623	1.397094431	
k1	0.4321	0.4469	0.7700	
k2	0.5459	0.6096	0.5652	
k3	0.8230	0.7444	0.4657	
Range (R)	0.3909	0.2976	0.3043	
Optimized result	A3B3C1			
Significance of factors	A > C > B			

Table 6
Analysis of ranges of orthogonal results (DPBH).

Trial No.	A	B	C	DPBH
1	1	1	1	0.3541
2	1	2	3	0.3684
3	1	3	2	0.2249
4	2	1	3	0.5550
5	2	2	2	0.2871
6	2	3	1	0.1722
7	3	1	2	0.4641
8	3	2	1	0.2871
9	3	3	3	0.1770
K1	0.947368421	1.373205742	0.813397129	
K2	1.014354067	0.942583732	0.976076555	
K3	0.928229665	0.574162679	1.100478469	
k1	0.3158	0.4577	0.2711	
k2	0.3381	0.3142	0.3254	
k3	0.3094	0.1914	0.3668	
Range (R)	0.0287	0.2663	0.0957	
Optimized result	A2B1C3			
Significance of factors	B > C > A			

4. Conclusions

This study validates a CFD-DEM model by comparing the simulation results with existing experimental data. Synfrac software is used to generate a rough fracture. The primary focus is investigating micro-internal mechanisms of proppant transport in narrow rough fractures and analyzing the flow regimes of blocky dunes using pressure drop and force analysis. The underlying influence mechanisms are investigated by varying injection velocity, fracture inclination angle, and fluid viscosity. The major findings of this study are summarized as follows:

Unlike continuous dunes found in planar fractures, blocky dunes in rough fractures exhibit distinct characteristics. Specifically, the drag force experienced during the blocky dune development process is generally larger. This process can be divided into two periods: the settlement-dominant and scour-dominant stages, representing two main impact mechanisms. Overall, there is an initial decrease in drag force followed by an increase.

A larger injection velocity results in a longer dune, larger drag force, and pressure drop due to the greater velocity difference from the static dune. However, it also leads to a lower particle–particle force, indicating reduced particle interaction and better transport efficiency.

Fracture inclination significantly affects dune shape. When the inclination is closer to horizontal, longer and lower dunes are formed, corresponding to lower drag force and pressure drop. Additionally, lower particle–particle force indicates better transport efficiency.

Injecting high-viscosity fluid can expand the dune length but reduce its height. It also results in a larger dimensionless drag force and pressure drop. Increasing the fluid viscosity makes the curve change characteristics less obvious. There is even a monotone trend in dimensionless viscosity of 9. There are two ways to improve transport efficiency in microscale mechanisms. One is to reduce particle–particle interaction forces and the other to increase settling time. Increasing viscosity in this article falls into the latter category.

Through the orthogonal test method, it can be found that the incline angle has the most significant impact on dimensionless proppant bank length (DPBL) and injection velocity has the most important impact on dimensionless proppant bank height (DPBH).

CRediT authorship contribution statement

Zhi-Chao Yang: Writing – original draft, Validation, Formal analysis, Data curation, Conceptualization. **Meng-Meng Zhou:** Writing – review & editing, Project administration, Methodology, Funding acquisition, Conceptualization. **Wen-Zhao-Yang Xie:** Supervision, Software, Resources, Investigation. **Xian-Zhi Song:** Writing – review & editing, Visualization, Funding acquisition, Formal analysis, Conceptualization. **Zheng-Ming Xu:** Writing – review & editing, Resources, Funding acquisition.

Declaration of competing interest

The authors declare that they have no known competing financial interests or personal relationships that could have appeared to influence the work reported in this paper.

Acknowledgments

The authors are grateful to the National Natural Science Foundation of China (Grant No. 52274019), Science Foundation of China University of Petroleum, Beijing (No. 2462022QNXZ004), Distinguished Young Foundation of Natural Science Foundation of China (No. 52125401), and National Key Laboratory of Petroleum Resources and Engineering, China University of Petroleum, Beijing (No. PRE/indep-3-2306) for the financial support and the use of high-performance computational facilities.

References

Akhshik, S., Behzad, M., Rajabi, M., 2016. CFD-DEM simulation of the hole cleaning process in a deviated well drilling: The effects of particle shape. Particuology 25 (2), 72–82. https://doi.org/10.1016/j.partic.2015.02.008.

An, S., Hasan, S., Erfani, H., et al., 2020. Unravelling effects of the pore-size correlation length on the two-phase flow and solute transport properties: GPU-based pore-network modeling. Water Resour. Res. 56 (8). e2020WR027403. https://doi.org/10.1029/2020WR027403.

Ba Geri, M., Imqam, A., Dunn-Norman, S., 2018. Proppant transport behavior in inclined versus vertical hydraulic fractures: An experimental study. In: SPE/AAPG Eastern Regional Meeting. D043S006R005. https://doi.org/10.2118/191813-18erm-ms.

Bai, B., Liang, T., Zhang, M., et al., 2021. Numerical solution of proppant transport and distribution in tortuous and uneven fractures. In: Proceedings of the 2021 Asia Pacific Unconventional Resources Technology Conference. https://doi.org/10.15530/ap-urtec-2021-208299.

Barboza, B.R., Chen, B., Li, C., 2021. A review on proppant transport modelling. J. Petrol. Sci. Eng. 204, 108753. https://doi.org/10.1016/j.petrol.2021.108753.

Basiuk, L., Roschzttardtz, F.I., Fernández, M.E., et al., 2022. Proppant transport in scaled experiments: Effect of drainage configuration and fracture wall roughness. J. Petrol. Sci. Eng. 208, 109433. https://doi.org/10.1016/j.petrol.2021.109433.

Budiman, O., Alajmei, S., Bahri, A., et al., 2025. A review of proppant transport and distribution in slickwater fracturing. Arabian J. Sci. Eng. 50 (7), 5303–5322. https://doi.org/10.1007/s13369-024-09938-y.

Chen, B., Barboza, B.R., Sun, Y., et al., 2022. A review of hydraulic fracturing simulation. Arch. Comput. Methods Eng. 29 (4), 1–58. https://doi.org/10.1007/s11831-021-09653-z.

Chun, T., Li, Y., Wu, K., 2020. Comprehensive experimental study of proppant transport in an inclined fracture. J. Petrol. Sci. Eng. 184, 106523. https://doi.org/10.1016/j.petrol.2019.106523.

Detournay, E., 2016. Mechanics of hydraulic fractures. Annu. Rev. Fluid Mech. 48 (1), 311–339. https://doi.org/10.1146/annurev-fluid-010814-014736.

Feng, Y., Li, G., Meng, Y., Guo, B., 2018. A novel approach to investigating transport of lost circulation materials in rough fracture. Energies 11 (10), 2572. https://doi.org/10.3390/en11102572.

Gidaspow, D., 1994. Multiphase Flow and Fluidization: Continuum and Kinetic Theory Descriptions. Academic Press.

Gong, F., Huang, H., Babadagli, T., et al., 2023. A resolved CFD-DEM coupling method to simulate proppant transport in narrow rough fractures. Powder Technol. 428, 118778. https://doi.org/10.1016/j.powtec.2023.118778.

Gui, N., Fan, J.R., Luo, K., 2008. DEM–LES study of 3-D bubbling fluidized bed with immersed tubes. Chem. Eng. Sci. 63 (14), 3654–3663. https://doi.org/10.1016/j.ces.2008.04.038.

Guo, T.K., Luo, Z.L., Zhou, J., et al., 2022. Numerical simulation on proppant migration and placement within the rough and complex fractures. Pet. Sci. 19 (5), 2268–2283. https://doi.org/10.1016/j.petsci.2022.04.010.

Huang, H., Babadagli, T., Li, Andy, et al., 2018. Visual analysis on the effects of fracture-surface characteristics and rock type on proppant transport in vertical fractures. SPE Hydraulic Fracturing Technology Conference and Exhibition. D011S002R002. https://doi.org/10.2118/189892-ms.

Huang, H., Babadagli, T., Li, H., et al., 2020. A visual experimental study on proppants transport in rough vertical fractures. Int. J. Rock Mech. Min. Sci. 134, 104446. https://doi.org/10.1016/j.ijrmms.2020.104446.

Huang, H., Babadagli, T., Li, H., et al., 2017. A quantitative and visual experimental study: Effect of fracture roughness on proppant transport in a vertical fracture. In: SPE Eastern Regional Meeting. D023S001R001. https://doi.org/10.2118/187520-ms.

Huang, H., Zheng, Y., Wang, Y., et al., 2024. Characteristics of proppant transport and placement within rough hydraulic fractures. Petrol. Explor. Dev. 51 (2), 453–463. https://doi.org/10.1016/s1876-3804(24)60036-4.

Kern, L.R., Perkins, T.K., Wyant, R.E., 1959. The mechanics of sand movement in fracturing. J. Petrol. Technol. 11 (7), 55–57. https://doi.org/10.2118/1108-g.

Kou, R., Moridis, G.J., Blasingame, T.A., 2018. Analysis and modeling of proppant transport in inclined hydraulic fractures. In: SPE Hydraulic Fracturing Technology Conference and Exhibition. D011S002R001. https://doi.org/10.2118/189856-ms.

Kuang, S., Zhou, M., Yu, A., 2020. CFD-DEM modelling and simulation of pneumatic conveying: A review. Powder Technol. 365, 186–207. https://doi.org/10.1016/j.powtec.2019.02.011.

Kuang, S.B., Yu, A.B., Zou, Z.S., 2009. Computational study of flow regimes in vertical pneumatic conveying. Ind. Eng. Chem. Res. 48 (14), 6846–6858. https://doi.org/10.1021/ie900230s.

Li, J., Han, X., He, S., et al., 2024a. Effect of proppant sizes and injection modes on proppant transportation and distribution in the tortuous fracture model. Particuology 84, 261–280. https://doi.org/10.1016/j.partic.2023.07.002.

Li, J., He, S., Wu, M., et al., 2023. A comprehensive review of the proppant transportation in different simplified fracture models: Experimentation, modeling, and prospects. Geoenergy Sci. Eng. 228, 211974. https://doi.org/10.1016/j.geoen.2023.211974.

Li, J., Kuang, S., Huang, F., et al., 2024b. CFD-DEM approach to study the proppant transport and placement under different perforation conditions in tortuous hydraulic fractures. SPE J. 29 (1), 277–298. https://doi.org/10.2118/217472-pa.

Li, J., Liu, P., Kuang, S., et al., 2021. Visual lab tests: proppant transportation in a 3D printed vertical hydraulic fracture with two-sided rough surfaces. J. Petrol. Sci. Eng. 196, 107738. https://doi.org/10.1016/j.petrol.2020.107738.

Li, N., Li, J., Zhao, L., et al., 2017. Laboratory testing on proppant transport in complex-fracture systems. SPE Prod. Oper. 32 (4), 382–391. https://doi.org/10.2118/181822-pa.

Li, P., Zhang, X., Lu, X., 2018. Numerical simulation on solid-liquid two-phase flow in cross fractures. Chem. Eng. Sci. 181, 1–18. https://doi.org/10.1016/j.ces.2018.02.001.

Li, Y., Mao, H., Yao, F., et al., 2011. The modeling of slurry friction loss of hydraulic fracturing. In: 2011 International Conference on Computational and Information Sciences, pp. 606–610. https://doi.org/10.1109/iccis.2011.295.

Liu, B., Kumar, D., Ghassemi, A., 2025. Modeling proppant transport and settlement in 3D fracture networks in geothermal reservoirs. Geothermics 125, 103176. https://doi.org/10.1016/j.geothermics.2024.103176.

Lv, M., Guo, T., Jia, X., et al., 2024. Study on the pump schedule impact in hydraulic fracturing of unconventional reservoirs on proppant transport law. Energy 286, 129569. https://doi.org/10.1016/j.energy.2023.129569.

Ogilvie, S.R., Isakov, E., Glover, P.W.J., 2006. Fluid flow through rough fractures in rocks. II: A new matching model for rough rock fractures. Earth Planet Sci. Lett. 241 (3–4), 454–465. https://doi.org/10.1016/j.epsl.2005.11.041.

Qu, H., Liu, Y., Lin, H., et al., 2022. 3D CFD-DEM simulation and experiment on proppant particle-fluid flow in a vertical, nonplanar fracture with bends. Int. J. Multiphas. Flow 146, 103873. https://doi.org/10.1016/j.ijmultiphaseflow.2021.103873.

Qu, H., Tang, S., Liu, Z., et al., 2021. Experimental investigation of proppant particles transport in a tortuous fracture. Powder Technol. 382, 95–106. https://doi.org/10.1016/j.powtec.2020.12.060.

Ravelet, F., Bakir, F., Khelladi, S., et al., 2013. Experimental study of hydraulic transport of large particles in horizontal pipes. Exp. Therm. Fluid Sci. 45, 187–197. https://doi.org/10.1016/j.expthermflusci.2012.11.003.

Sahai, R., Moghanloo, R.G., 2019. Proppant transport in complex fracture networks–A review. J. Petrol. Sci. Eng. 182, 106199. https://doi.org/10.1016/j.petrol.2019.106199.

Song, X., Yang, Z., Zhou, M., Xu, Z., Abderrahmane, H.A., et al., 2024. CFD-DEM simulation analysis of the effect of sweep stages on proppant placement within rough fracture. In: SPE Gas & Oil Technology Showcase and Conference. D021S025R001. https://doi.org/10.2118/219284-ms.

Suri, Y., Islam, S.Z., Hossain, M., 2019. A new CFD approach for proppant transport in unconventional hydraulic fractures. J. Nat. Gas Sci. Eng. 70, 102951. https://doi.org/10.1016/j.jngse.2019.102951.

Tang, P., Li, H., Zeng, J., 2022. Numerical investigation of transport behaviors of nonspherical proppants in hydraulic fracturing using CFD-DEM. Part. Sci. Technol. 40 (2), 207–218. https://doi.org/10.1080/02726351.2021.1930301.

Tong, S., Mohanty, K.K., 2016. Proppant transport study in fractures with intersections. Fuel 181, 463–477. https://doi.org/10.1016/j.fuel.2016.04.144.

Wen, Q., Wang, S., Duan, X., et al., 2016. Experimental investigation of proppant settling in complex hydraulic-natural fracture system in shale reservoirs. J. Nat. Gas Sci. Eng. 33, 70–80. https://doi.org/10.1016/j.jngse.2016.05.010.

Wen, Z., Zhang, L., Tang, H., et al., 2024. A review on proppant transport in complex fracture geometries. Petrol. Sci. Technol. 42 (25), 4626–4643. https://doi.org/10.1080/10916466.2023.2242396.

Xiao, B., Li, H., Wei, C., et al., 2025. Numerical simulation on the transport and displacement patterns of proppant in hydraulic fractures considering the effect of rough fracture surfaces. Processes 13 (2), 461. https://doi.org/10.3390/pr13020461.

Yamashiro, B.D., Tomac, I., 2022. Fracture roughness effects on slickwater proppant slurry settling attenuation. Powder Technol. 395, 516–533. https://doi.org/10.1016/j.powtec.2021.10.002.

Yang, Z., Zhou, M., Song, X., et al., 2024. Study of proppant plugging in narrow rough fracture based on CFD–DEM method. Powder Technol. 442, 119861. https://doi.org/10.1016/j.powtec.2024.119861.

Yin, B., Zhang, C., Wang, Z., et al., 2023. Proppant transport in rough fractures of unconventional oil and gas reservoirs. Petrol. Explor. Dev. 50 (3), 712–721. https://doi.org/10.1016/s1876-3804(23)60422-7.

Zhang, B., Pathegama Gamage, R., Zhang, C., et al., 2023. On the correlation between proppant addition strategy and distribution. Gas Sci. Eng. 117, 205060. https://doi.org/10.1016/j.jgsce.2023.205060.

Zhang, B., Pathegama Gamage, R., Zhang, C., et al., 2022. Hydrocarbon recovery: Optimized CFD-DEM modeling of proppant transport in rough rock fractures. Fuel 311, 122560. https://doi.org/10.1016/j.fuel.2021.122560.

Zheng, Y., Wang, H., Huang, H., et al., 2025a. CFD-DEM simulation of proppant transport under variable injection strategies in rough fracture network with supercritical CO_2. Powder Technol. 457, 120856. https://doi.org/10.1016/j.powtec.2025.120856.

Zheng, Y., Wang, H., Wang, B., et al., 2023. Effect of roughness characteristics of hydraulic fractures on the proppant transport using supercritical CO_2. Geoenergy Sci. Eng. 227, 211908. https://doi.org/10.1016/j.geoen.2023.211908.

Zheng, Y., Wang, H., Yang, B., et al., 2020. CFD-DEM simulation of proppant transport by supercritical CO_2 in a vertical planar fracture. J. Nat. Gas Sci. Eng. 84, 103647. https://doi.org/10.1016/j.jngse.2020.103647.

Zheng, Y., Wang, Z., Chen, H., et al., 2025b. Numerical simulation of proppant transport with multi-stage alternating injection in CO_2 hybrid fracturing. Powder Technol. 456, 120840. https://doi.org/10.1016/j.powtec.2025.120840.

Zhou, M., Kuang, S., Luo, K., et al., 2020. Modeling and analysis of flow regimes in hydraulic conveying of coarse particles. Powder Technol. 373, 543–554. https://doi.org/10.1016/j.powtec.2020.06.085.

Zhou, M., Kuang, S., Xiao, F., et al., 2021. CFD-DEM analysis of hydraulic conveying bends: Interaction between pipe orientation and flow regime. Powder Technol. 392, 619–631. https://doi.org/10.1016/j.powtec.2021.07.052.

Zhou, M., Wang, S., Kuang, S., et al., 2019. CFD-DEM modelling of hydraulic conveying of solid particles in a vertical pipe. Powder Technol. 354, 893–905. https://doi.org/10.1016/j.powtec.2019.07.015.

Zhou, M., Wang, S., Luo, K., et al., 2022. Three-dimensional modeling study of the oxy-fuel co-firing of coal and biomass in a bubbling fluidized bed. Energy 247, 123496. https://doi.org/10.1016/j.energy.2022.123496.

Zhou, M., Yang, Z., Xu, Z., et al., 2024. CFD-DEM modeling and analysis study of proppant transport in rough fracture. Powder Technol. 436, 119461. https://doi.org/10.1016/j.powtec.2024.119461.

Zhou, Z.Y., Kuang, S.B., Chu, K.W., et al., 2010. Discrete particle simulation of particle–fluid flow: Model formulations and their applicability. J. Fluid Mech. 661, 482–510. https://doi.org/10.1017/s002211201000306x.